PAPER
Zhenxing Chen, Ziwei Li *et al.*
Improved out-of-plane thermal conductivity of boron nitride
nanosheet-filled polyamide 6/polyethylene terephthalate
composites by a rapid solidification method

Materials Advances

PAPER

Improved out-of-plane thermal conductivity of boron nitride nanosheet-filled polyamide 6/polyethylene terephthalate composites by a rapid solidification method†

Qingchong Xu,[ab] Zhenxing Chen, [iD] *[abc] Xinxin Li,[a] Jiaxin Hu,[a] Yanling Liao,[ab] Yongfeng Liu,[a] Long Li,[b] Shiyang Wei[b] and Ziwei Li [iD] *[d]

High thermal conductivity of insulating polymer composite material can effectively solve the heat dissipation problem associated with electronic equipment. In this work, we obtained modified boron nitride nanosheets (m-BNNSs) by ultrasonic exfoliation and modification. The surface was successfully grafted with organic functional groups that promoted the compatibility between filler and matrix. Orienting them along the in-plane during the preparation process was facilitated by the anisotropy of BNNSs, which resulted in poor out-of-plane thermal conductivity. Herein, m-BNNSs were uniformly and randomly orientated in the polyamide 6/polyethylene terephthalate (PET/PA6) matrix by a simple strategy of a rapid solidification method including solution mixing, rapid solidification, and hot pressing. The randomly orientated m-BNNSs increased the thermal conductivity of the PA6/PET composite film as high as 3.28 W $(m^{-1} K^{-1})$ at a filler loading of 55 wt%, which is 64% higher than that of directly hot-pressed h-BN/PA6/PET composite film. With the increase in filler, the m-BNNS/PET/PA6 composite film exhibited excellent thermal stability as compared to pure PET/PA6 matrix. Such excellent performance indicates that there is a great deal of potential for this composite to be used in thermal management. Non-equilibrium molecular dynamics (NEMD) simulations showed that the increase in the numbers of boron nitride nanosheet (BNNS) layers and the orientation change from vertical heat flow to parallel heat flow can effectively increase the phonon density of states overlap area of BNNSs and PA6/PET, thereby enhancing the interfacial thermal conductance (G_k).

1. Introduction

With the increasing level of sophistication in the electronics industry, electronic components are being developed in the direction of integration, densification, and miniaturization, and therefore, there are higher requirements for the thermal diffusion efficiency of thermal interface materials (TIMs), especially in 5G communication.[1,2] Although polymers have been widely used as TIMs, their intrinsic thermal conductivity is very low due to their amorphous region, which causes a scattering

phenomenon of the lattice vibration during transmission.[3,4] Considering the heat resistance and flexibility, polyamide 6 (PA6) and polyethylene terephthalate (PET) are satisfactory choices for thermal conductive matrixes.[5–7]

To overcome the problem of low thermal conductivity by a matrix, the most common methods tend to add high thermal conductive fillers. Currently, the high thermal conductive fillers that have been studied mainly include carbon fillers (such as graphene,[8–10] carbon fiber,[11] and carbon nanotubes[12]), and ceramic fillers (such as alumina,[13] aluminum nitrite,[14,15] boron nitrite,[16–19] and silicon carbide[20–22]). Polymer-based thermal conductive composites are commonly prepared using only the hot pressing method,[23,24] in which the two-dimensional (2D) thermal conductive fillers orientate parallel to the horizontal direction of the composite film and then cause poor thermal conductivity in the vertical direction. For example, Yu *et al.*[23] prepared hexagonal boron nitride (hBN)/thermoplastic polyurethane (TPU) composite by a hot pressing method, with in-plane and out-of-plane thermal conductivity to 10 and 1.5 W $(m^{-1} K^{-1})$ at 50 wt% boron nitride nanosheet (BNNS) loading, respectively.

a School of Chemical Engineering and Technology, Sun Yat-Sen University, Zhuhai 519082, P. R. China

b School of Chemistry and Environment, Jiaying University, Meizhou 514015, P. R. China

c The Key Laboratory of Low-Carbon Chemistry & Energy Conservation of Guangdong Province, Guangzhou 510275, P. R. China

d College of Materials Science and Engineering, Guilin University of Technology, Guilin 541000, P. R. China. E-mail: 2764927916@qq.com

To increase the out-of-plane thermal conductivity of composites, the presence of 2D thermal conductive fillers vertically or randomly orientated in the matrix is very important.

Graphene-like hexagonal boron nitride (h-BN) is an ideal thermal conductive filler for polymer matrix composites because of its favorable electrical insulation, thermal conductivity, and lubricity.[25,26] As a typical 2D material, strong anisotropic thermal conductivity has been observed for h-BN (in-plane direction (600 W $(m^{-1} K^{-1})$), out-of-plane direction (30 W $(m^{-1} K^{-1})$)). To increase the out-of-plane thermal conductivity, constructing a 3D network with vertically arranged fillers,[1,27,28] slicing up with vertical orientation and then compact packing,[29] magnetic field induction[30] and a freeze-drying technique[31] have been suggested.

Wu et al.[32] prepared a three-dimensional (3D)-BN scaffold composite material containing randomly oriented boron nitride using the ice template method, and the out-of-plane thermal conductivity was 1.42 W $(m^{-1} K^{-1})$ at 13.41 vol% filler loading. However, the method is complex and difficult to implement on a massive scale. Pan et al.[33] and Chen et al.[34] effectively disrupted the arrangement of 2D materials along the lateral direction during the compression process by adding AlN and Al_2O_3 particles, respectively, thus increasing the out-of-plane thermal conductivity of the composite. Due to the different structures and morphologies of different fillers, the synergistic effect of the heat transfer properties may be disrupted.

Therefore, it is urgent to develop a simple process to randomly distribute a single filler BN in order to expand the application of composite films.

Functionalization of heat-conductive fillers can promote their dispersion in the polymer matrix and reduce phonon loss at the interface, thus enhancing the interface heat transfer between the polymer matrix and fillers.[35-38] Because h-BN possesses few functional groups[39] at its edge, such as hydroxyl (–OH) and amino (–NH$_2$), the introduction of additional –OH functional groups at the edge of the h-BN lamellae would increase the possibility of h-BN modification.

Liu et al.[40] prepared epoxy resin-based composites containing hydroxylated BNNSs modified with triethoxysilane (APTES), and they exhibited a 95% improvement in thermal conductivity over unexfoliated and unmodified hBN/epoxy composite at their filler content of 40 wt%. Recent extensive studies on liquid-phase exfoliation were conducted,[41-43] and a large specific surface area and a greater abundance of edge groups were noted for exfoliated BNNSs as compared to the raw material h-BN. It is time-consuming to perform low-intensity liquid-phase exfoliation, and low yields are obtained. Therefore, the use of strong ultra-sound for exfoliation is worth trying.

In this work, a rapid solidification method including solution mixing, rapid solidification, and hot pressing is put forward to prepare thermally conductive insulating composites, in which modified boron nitride nanosheets (m-BNNSs) are in a
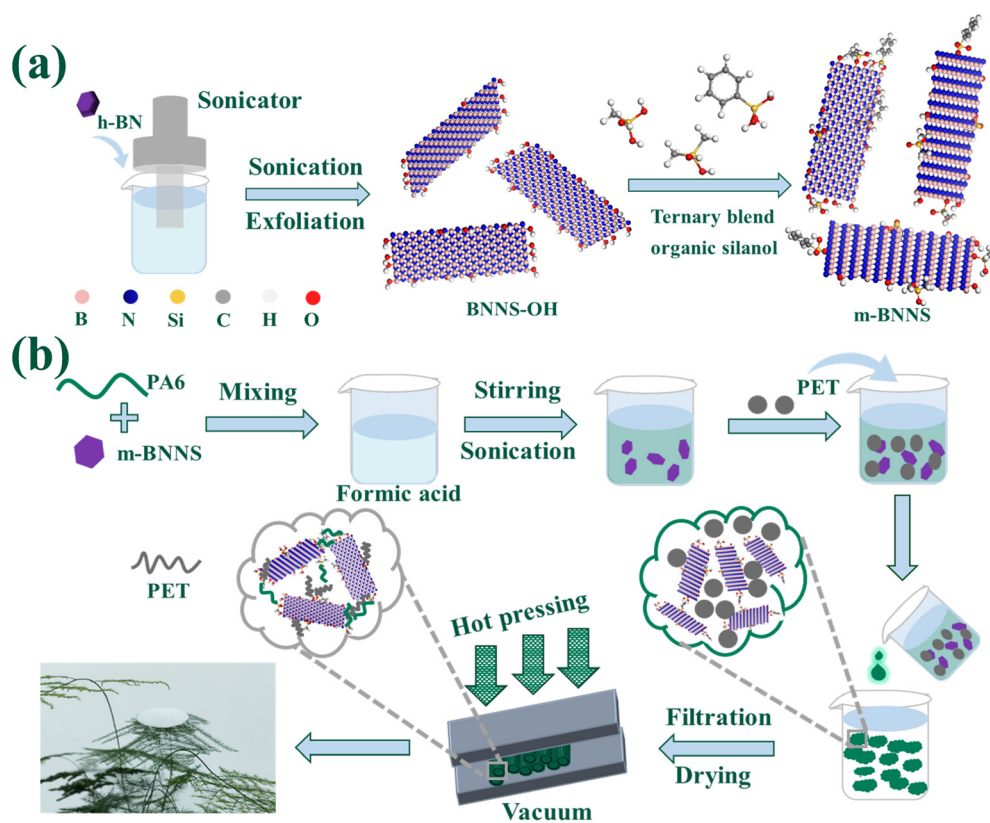

Fig. 1 Schematic diagram: (a) preparation of ternary blend organic silanol–modified BNNSs; (b) preparation of randomly oriented m-BNNS/PA6/PET composites through a rapid solidification method.

randomly oriented state. First, h-BN was treated by ultrasonic exfoliation and surface modification to obtain m-BNNSs to enhance the compatibility between the filler and matrix. Second, m-BNNS/PA6/PET composite films were prepared by the rapid solidification method. This technology can be utilized to produce high thermal conductivity composites on a massive scale. Non-equilibrium molecular dynamics (NEMD) was used to study the interfacial thermal conductance (G_k) between the thermal conductive filler and the PA6/PET matrix on a microscopic scale. The influence of the number and orientation of the BNNS layers on the G_k was explored, which might provide theoretical guidance for increasing the interfacial thermal conductivity of fillers and matrix.

2. Experimental section

2.1 Materials

h-BN (size 5–10 μm, purity >99%) was purchased from Qinhuangdao ENO High-Tech Material Development Co., Ltd (Shandong, China). PA6 and PET were purchased from Dupont China Holding Co., Ltd. Ternary blend organic silanol was synthesized in the laboratory.

2.2 Exfoliation and functionalization of BNNSs

Boron nitride nanosheets with hydroxyl groups (BNNS-OH) were prepared from micron raw material h-BN by ultrasonic exfoliation in water and then modified by ternary blend organic silanol, as shown in Fig. 1(a). First, h-BN and deionized water were mixed and treated in a homemade high-energy ultrasonic instrument (5 kW m^{-2}) for 12 h to obtain BNNS-OH. Then, the ternary blend organic silanol was added to the mixed slurry of BNNS-OH and ethyl alcohol and reacted at 80 °C for 1 h to obtain organic silanol-modified m-BNNSs.

2.3 Preparation of m-BNNS/PA6/PET composite films

The m-BNNS/PA6/PET ternary composite films were prepared through a rapid solidification method that included solution mixing, rapid solidification, and hot pressing, as shown in Fig. 1(b). After the m-BNNSs had been uniformly dispersed in the PA6 solution (using formic acid as the solvent), the PET powder was added to the slurry in a mass ratio of PA6/PET = 5/1. Then, the m-BNNS/PA6/PET slurry was poured into deionized water, in which PA6 rapidly coagulated into solid particle composites combined with PET powder and m-BNNSs. After filtering, and repeatedly washing and drying, an m-BNNS/PA6/PET composite film was obtained by hot pressing with control of PET in the molten state. Herein, composite films with m-BNNS loading of 0, 10, 20, 30, 50, and 55 wt% were prepared. Furthermore, h-BN/PA6/PET composite films were also prepared by the rapid solidification method. For comparison, directly hot-pressed h-BN/PA6/PET composite films were prepared after h-BN, PA6, and PET were evenly mixed in a v-type mixer.

2.4 Characterization

The size of h-BN and the cross-sections of composite films were characterized by scanning electron microscopy (SEM, JSM-IT200, Japan). The morphology of the BNNSs was observed by atomic force microscopy (AFM, Bruker Dimension Icon, Germany), field emission scanning electron microscopy (FE-SEM, Apreo 2 S, USA) and transmission electron microscopy (TEM, HT7800, Japan). A laser particle size analyzer was used to measure the diameter of the powder before and after BNNS exfoliation (Anton Paar, PSA 1190L, France). The functional groups of powder in the range of 500 to 4000 cm^{-1} were analyzed with a Fourier transform infrared (FTIR) spectrometer (Spectrum Two, USA). The microstructures of the powders and composite films were tested by X-ray diffraction (XRD, Ultima IV, Japan) using Cu Kα radiation with a 2θ range of 10–80° at a scan rate of 10° min^{-1}. The elemental composition and chemical states of the sample surface were analyzed through X-ray photoelectron spectroscopy (XPS, Thermo Scientific K-Alpha, USA).

Furthermore, the microstructures of the powders were characterized by a Raman spectroscope (Raman, WITecalpha300R, Germany) in a wavenumber range of 500–3500 cm^{-1} with a 532 nm laser. The surface temperature of the composite films was captured by an infrared camera (FLIR SC325, USA). The thermal conductivity of the composite films was measured with a thermal conductivity tester (DRL-III, China). Thermogravimetric analysis (TGA) of powders and composite films was performed using a thermogravimetric analyzer (TG209F1 Libra, Germany) at a heating rate of 10 °C min^{-1} from 25 to 800 °C in nitrogen. The glass transition temperature and melting temperature of the composite films were measured by differential scanning calorimetry (DSC, TA DSC2500, USA).

2.5 NEMD simulations

The NEMD method was used to study the heat transfer behavior between BNNSs and the PA6/PET matrix. For BNNS/PA6/PET composites, two types of interface models were established (a schematic diagram is shown in a). One consists of the BNNS surface aligned perpendicularly to the heat flow, and then the effect of BNNSs varying from the second layer to the eighth layer on the G_k was studied. The second model consists of the BNNS surface aligned parallel to the heat flow. BNNSs present as an eight-layered structure, and therefore, the dimensions in all directions are exactly equal to the eight-layer BNNSs perpendicular to the heat flow plane. Through the study of two eight-layer BNNS models, the effect of filler orientation on the G_k can be explored.

In this work, the Large-scale Atomic/Molecular Massively Parallel Simulator (LAMMPS) package was used to perform all molecular dynamics (MD) simulations. In the above models, the size of BNNSs is specified as 2.61×2.76 nm, PET possesses a hexameric molecular structure,[44] and the PA6 molecule contains six monomers.[45] The PCFF potential[46–49] was used to describe the atomic interactions in the PA6/PET system, and the Tersoff potential[50–53] was used to describe the interactions between BNNS layers. The interactions between the layers of BNNSs, BNNS/PET, and BNNS/PA6 are described by the

Lennard-Jones (LJ) potential as follows:

$$U(r_{ij}) = 4\varepsilon_{ij}\left[\left(\frac{\sigma_{ij}}{r_{ij}}\right)^{12} - \left(\frac{\sigma_{ij}}{r_{ij}}\right)^{6}\right] \qquad (1)$$

where r_{ij} is the distance between atom i and atom j; ε_{ij} is energy constant; σ_{ij} is distance constant. The LJ potential parameters between BNNS layers[54,55] are $r = 0.33$ nm and $\varepsilon = 4$ meV. The structure of the constructed model was optimized by the smart algorithms. The optimized model was subjected to kinetic equilibrium at a constant atomic number, volume, and temperature ensemble (*NVT* ensemble) with a Nosé–Hoover thermostat at 300 K for 500 ps. To prevent energy exchange between particles and the outside world, fixed layers were set at both ends of the model. A hot source and cold sink were set up inside the fixed layer. A Langevin thermostat[56–58] was used to maintain the temperature in the hot source and cold sink at a preset 330 K and 270 K, respectively. Then, the system was switched to the *NVE* (constant volume and no thermostat) ensemble for 500 ps equilibrium, which can form a stable heat flux inside the model. After that, a 1 ns NEMD simulation was then performed to output data for calculation. The time step for all simulations in this study was chosen to be 0.25 fs. The dynamic change in the energy in the hot source and cold sink and the temperature difference (Fig. S5, ESI†) formed at the interface were calculated in four counts. From the definition of heat flux and Fourier's law, and can be calculated by:

$$J = \frac{(\Delta E_{hot} + \Delta E_{cold})}{2A\Delta t} \qquad (2)$$

$$G_k = J/\Delta T \qquad (3)$$

where J is the heat flux; ΔE_{hot} and ΔE_{cold} are the energy changes in the hot source and cold sink, respectively; A denotes the cross-sectional area; Δt is the simulation time.

3. Results and discussion

3.1 Characterization of BNNS-OH and m-BNNSs

The intrinsic thermal conductivity of h-BN depends on its vertical thickness.[40,53,59] Therefore, it is meaningful to obtain BNNSs by ultrasonic exfoliation of raw micron h-BN. Fig. 2(a) and Fig. S1a (ESI†) present the SEM image of h-BN and the corresponding particle size distribution, respectively, which show a flat surface with clear edges and an average transverse size of approximately 11 μm. Fig. 2(b) and (c), and Fig. S1b (ESI†) present the AFM images of BNNSs, which indicate approximately 3.8 nm thickness and approximately 4 μm average particle size. Theoretically, the interlayer spacing of BNNSs is 0.33 nm,[60] and therefore, the as-prepared BNNS is relatively thin. Fig. 2(d) presents an FE-SEM image of a BNNS, which shows that it maintains complete morphology under small size. Fig. 2(e) and (f) present the TEM image, demonstrating the ultra-thin and transparent characteristics of a BNNS with sharp outlines. The above results indicate that BNNSs were successfully prepared by ultrasonic exfoliation, and the transverse size of BNNSs was decreased as a consequence of ultrasonic oscillation.

The FT-IR spectra of raw h-BN, exfoliated BNNS-OH, and functionalized m-BNNSs were analyzed, and the result is shown in Fig. 3(a). Three curves all have strong characteristic peaks at 811 cm^{-1} and 1380 cm^{-1}, corresponding to the stretching vibration in-plane of BN and bending vibration out-of-plane
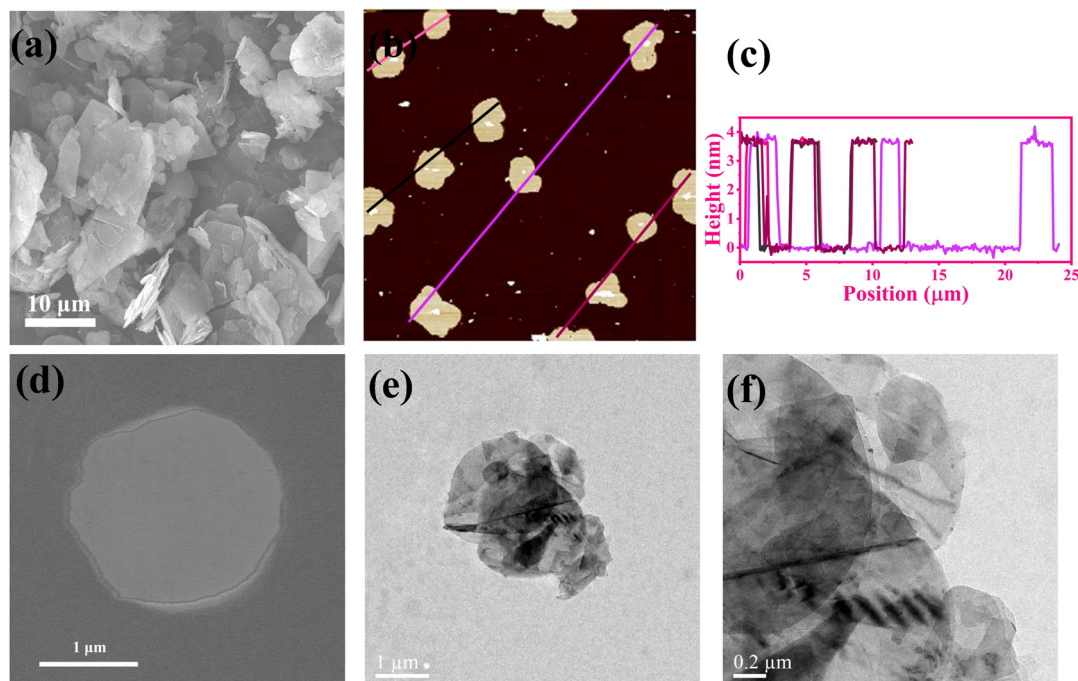

Fig. 2 Morphology and microstructure of BN. (a) SEM image of h-BN; (b) AFM image of BNNSs exfoliated from h-BN; (c) size statistics for BNNSs; (d) FE-SEM micrograph of BNNSs; and (e), (f) TEM images of BNNSs.

of BN, respectively.[37] BNNS-OH exhibited a characteristic absorption peak of –OH at 3415 cm^{-1},[16] which is significantly stronger than that of h-BN, indicating that large amounts of hydroxyls were generated on the BNNS surface after an ultrasound treatment. Comparison of h-BN by reaction with organic silanol (Fig. S2, ESI†) and m-BNNSs modified by the ternary blend organic silanol (Fig. S3, ESI†) show characteristic absorption peaks at 2945 cm^{-1} and 2860 cm^{-1}, corresponding to the asymmetric and symmetric stretching vibrations of –CH$_2$–, respectively.[61] In addition, a stretching vibration absorption peak of –Si–O– appeared near 1113 cm^{-1},[62] which infers that the organic silanol was successfully coated on the surface of BNNS-OH.

In Fig. 3(b), the XRD patterns of h-BN, BNNS-OH, and m-BNNSs all show a series of diffraction peaks, corresponding to the (002), (100), (101), (102), and (004) lattice planes of the hexagonal BN (JCPDS: 45-0893), which shows that the crystal form of the particles does not change after ultrasonic exfoliation and ternary blend organic silanol modification. The (002) and (004) diffraction intensities of ultrasonically exfoliated BNNS-OH are weaker than those of h-BN, which may be due to the reduction in the number of BNNS layers[63] and the smaller lateral dimension.[16] Compared with BNNS-OH, the intensity of the (002) peak of m-BNNS decreased after modification, indicating that the ternary blend organic silanol had been successfully grafted to the surface of BNNSs.

Fig. 4(a) shows the XPS spectra of h-BN, BNNS-OH, and m-BNNSs. The XPS spectrum of m-BNNSs reveals the co-existence of O, N, C, B, and Si elements. Compared with h-BN, the O content in the BNNS-OH spectrum is increased and two Si peaks appear for m-BNNSs, which is consistent with the results of FT-IR spectroscopy. This demonstrates that the exfoliated BNNSs produced more –OH and successfully reacted with the ternary blend organic silanol. The high-resolution XPS spectra for B1s and O1s in BNNS-OH and C1s and Si2p in m-BNNSs were fitted by the multimodal Gaussian method to confirm the connection of functional groups. The B1s spectrum (Fig. 4(b)) contains two fitted peaks at 190.4 and 191.0 eV, which are

attributed to the B–N and B–O bonds, respectively. The O1s spectrum (Fig. 4(c)) presents two fitted peaks at 532.6 and 533.5 eV, corresponding to O–H and O–B bonds, respectively. In addition, the C1s spectrum (Fig. 4(d)) shows four fitted peaks at 284.8, 285.8, 286.7, and 283.7 eV, corresponding to C–C, C–N, C–Si, and C–O bonds, respectively. The Si2p spectrum (Fig. 4(e)) includes four fitted peaks of Si–O–Si, Si–O–B, Si–OH, and Si–C at 103.6, 102.9, 102.3, and 100.8 eV, respectively.

These values are similar to those previously reported,[61,62,64] which confirms the successful bonding of BNNSs to silicone alcohol. To study the content of ternary blend organic silanol in m-BNNSs, thermogravimetric tests of h-BN and m-BNNSs were carried out. Fig. 4(f) presents the TGA curves for h-BN, BNNS-OH, and m-BNNSs. At 800 °C, the BNNS-OH residues were at 99.57 wt%, with the mass lost due to hydroxyl group oxidation. Different from h-BN and BNNS-OH, the m-BNNSs began weightlessness at 380 °C, and the weight loss rate at 800 °C was 1.07 wt%. The weight loss can be attributed to the decomposition of the organosilicon polymer. In Fig. S4 (ESI†), the Raman spectra for h-BN, h-BNNSs, and m-BNNSs all show similar characteristic G bands at 1366 cm^{-1}, which are due to the out-of-plane vibrations of boron and nitrogen atoms.[65,66] The intensity of the three peaks sequentially decreased due to exfoliation and modification, which is in agreement with a previous report.[67] According to the above results for XRD, XPS, TGA, and FT-IR and Raman spectroscopy, it can be concluded that ternary blend organic silanol successfully modified BNNS-OH.

3.2 Morphology and structure of composite films

In this work, h-BN/PET/PA6 (directly hot-pressed) composites were prepared by hot-pressing h-BN, PET, and PA6 after uniformly stirring them. The h-BN/PET/PA6 and m-BNNS/PET/PA6 composites were prepared by a rapid solidification method including solution mixing, rapid solidification, and hot pressing. To observe the orientation structure of thermally conductive fillers inside the composites, the cross-sections of the composites were observed by SEM. A typical layered structure of h-BN appears in the h-BN/PA6/PET (directly hot-pressed) composite
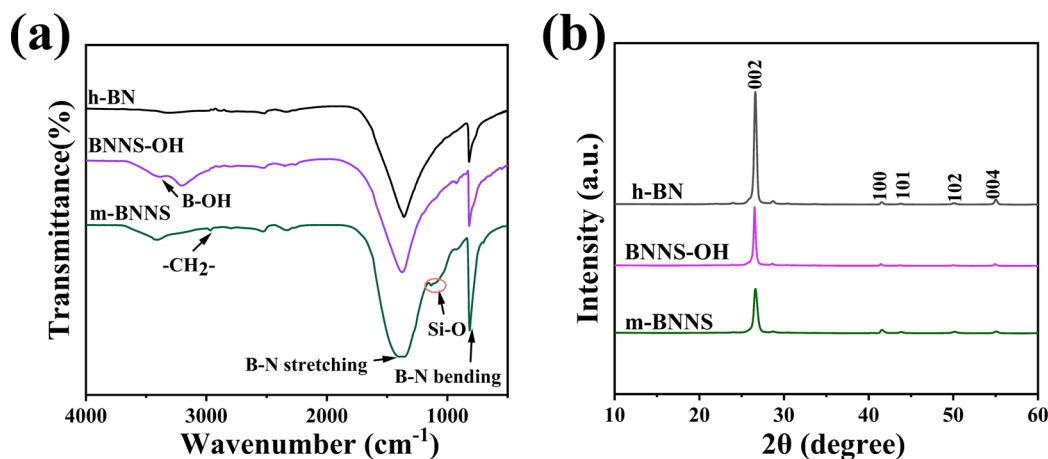

Fig. 3 (a) FT-IR spectra of raw h-BN, exfoliated BNNS-OH, and functionalized m-BNNSs; (b) XRD patterns.
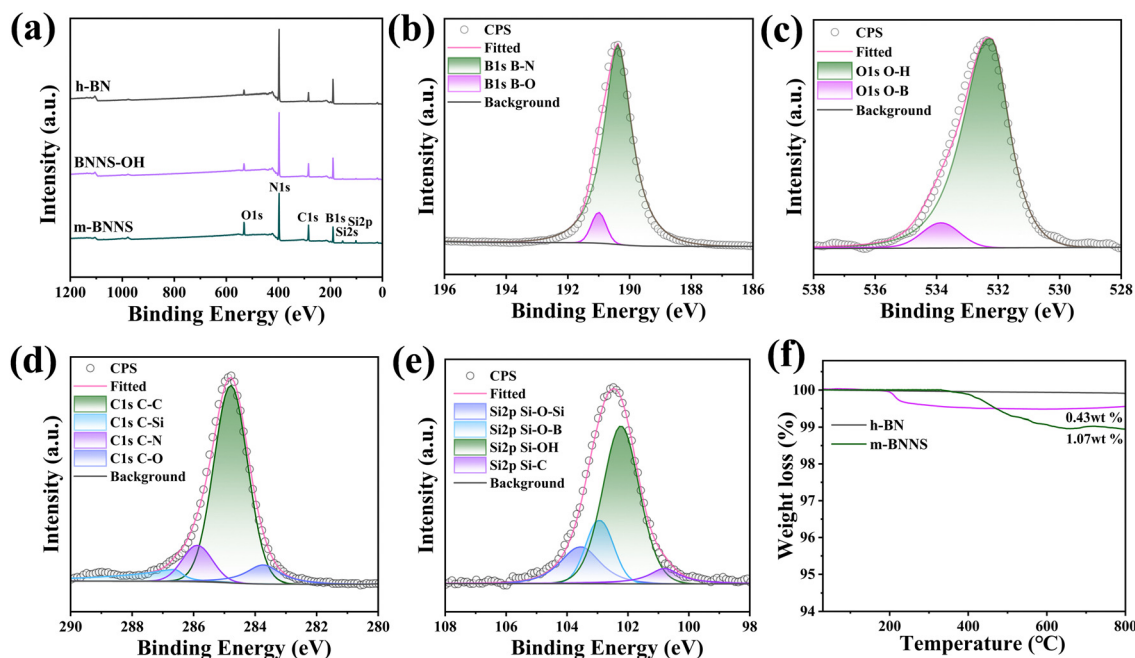
Fig. 4 (a) XPS of survey scans; high-resolution XPS analysis of (b) B 1s and (c) O 1s for BNNS-OH and (d) C 1s and (e) Si 2p for m-BNNSs. (f) TGA curves of h-BN and m-BNNSs.

film (shown in Fig. 5(a1)–(a3)), which is not conducive to the propagation of phonons in the out-of-plane direction. In contrast, the h-BN in the rapidly solidified h-BN/PA6/PET composite film (Fig. 5(b1)–(b3)) was randomly orientated, which is

conducive to the construction of a thermal network and enhances the thermal conductivity of the composite. Fig. 5(c1)–(c3) and (d1)–(d3) show that with the increase in filler loading, the rapidly solidified m-BNNS/PA6/PET composite film becomes increasingly
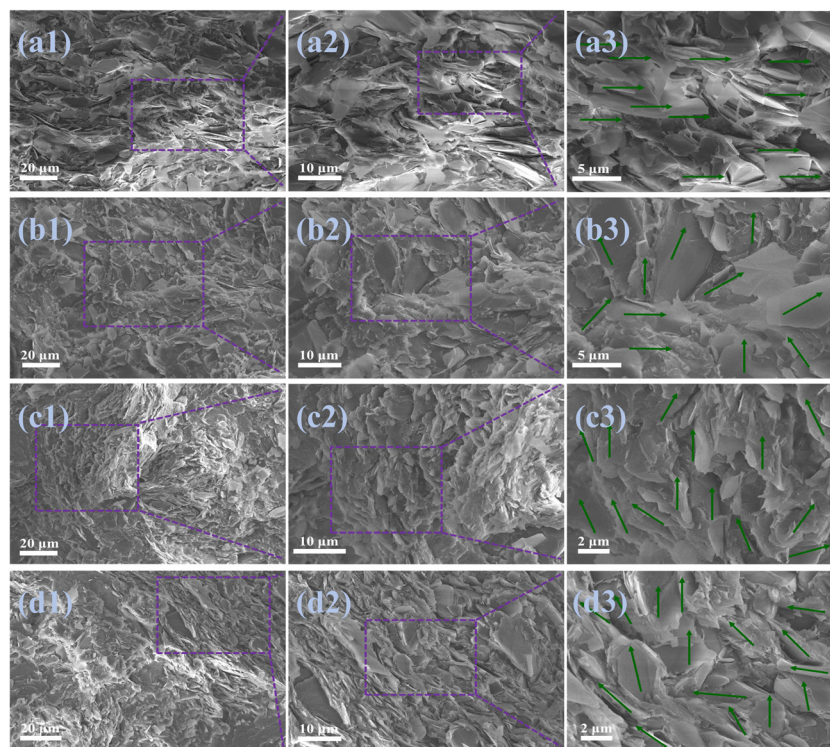

Fig. 5 Microstructure of the prepared h-BN and m-BNNS-filled PA6/PET composites. Cross-sectional morphologies of h-BN/PA6/PET (directly hot-pressed) composite film at filler loading of 55 wt% (a1)–(a3), h-BN/PA6/PET composite film at filler loading of 55 wt% (b1)–(b3), and m-BNNS/PA6/PET composite films at the filler loading of 40 wt% (c1)–(c3) and 55 wt% (d1)–(d3).

compact and appears to be more vertically distributed in m-BNNSs due to the small size and thinness of the m-BNNSs. Moreover, it was observed that the dispersion of m-BNNSs in the PA6/PET matrix was satisfactory and without agglomeration and voids, which indicates that the ternary blend organic silanol can improve the interaction between the filler and the matrix and reduce the interfacial thermal resistance.

To further characterize the orientation of fillers in the composite, different composite films were characterized by XRD (Fig. 6). Pure PA6/PET film is characterized by a typical amorphous nature. The (100) diffraction peak of h-BN almost disappeared in the 55 wt% h-BN/PA6/PET (directly hot-pressed) film, indicating that the fillers were aligned along the in-plane direction, which is not conducive to out-of-plane thermal conductivity. Compared with the h-BN/PA6/PET composite film, there was a lower I_{002}/I_{100} ratio for the m-BNNS/PA6/PET composite film at the same filler content, indicating that the degree of the random orientation of fillers increases, and the interior contains more vertically arranged BNNSs, which is conducive to the construction of thermal conductive networks and enhances the out-of-plane thermal conductivity of the composites. This is congruent with the SEM findings, where the above SEM and XRD results show that fabricating composite films with random filler orientation and using the rapid solidification method is easier than direct hot pressing.

3.3 Thermal conductivities and thermal properties of composites

Fig. 7(a) shows the thermal conductivity of the composites with different filler content. The thermal conductivity of composite film fabricated by the rapid solidification method is obviously higher than that produced by the direct hot-pressing method, and the thermal conductivity of the m-BNNS/PA6/PET composite is clearly higher than that of the h-BN/PA6/PET composite. When the filler loading was 55 wt%, the thermal conductivity of the m-BNNS/PA6/PET composite was 3.28 W $(m^{-1}$ $K^{-1})$, which was 30% higher than that of the h-BN/PA6/PET composite and 64% higher than that of the h-BN/PA6/PET (directly hot-pressed) composite. The first reason for this is that m-BNNSs are irregularly distributed in the matrix due to the process of rapid solidification, which is conducive to the propagation of out-of-plane phonons and promotes the formation of thermal conduction networks. The second reason is that the thickness of BNNSs is reduced and its intrinsic thermal conductivity is higher. The third reason is that, due to the low steric resistance of the ternary blend organic silanol, it acts as a bridge between BNNSs and PA6/PET, which increases the wettability and compatibility of the two phases and reduces phonon scattering at the interface. Fig. 7(b) depicts the change in thermal conductivity of the m-BNNS/PA6/PET composite film at filler loading of 55 wt% over 10 heating/cooling cycles. The thermal conductivity of the film is higher at 41 °C than that at 95 °C. However, this difference is very slight, inferring that the composite film possesses temperature stability.

To visualize the heat transfer efficiency of the three different types of composite films at filler loading of 55 wt%, the variations in the sample surface temperature with time during heating and cooling were recorded by an infrared thermal camera, and the results are shown in Fig. 8(a)–(d). During the heating process, square samples of h-BN/PA6/PET (directly hot-pressed), h-BN/PA6/PET, and m-BNNS/PA6/PET were placed on a hot plate (80 °C) (Fig. 8(a)) simultaneously from left to right (Fig. 8(a)). The surface temperature of all samples continuously increased with time, rising to the saturation temperature at 30 s. The heat rate was ranked as h-BN/PA6/PET (directly hot-pressed) < h-BN/PA6/PET < m-BNNS/PA6/PET (Fig. 8(a) and (b)).

Similarly, to investigate the heat dissipation process, all samples were placed on a hot plate at 80 °C for 15 min to achieve homogeneous temperatures, and then the surface temperature variations of these samples were measured as a
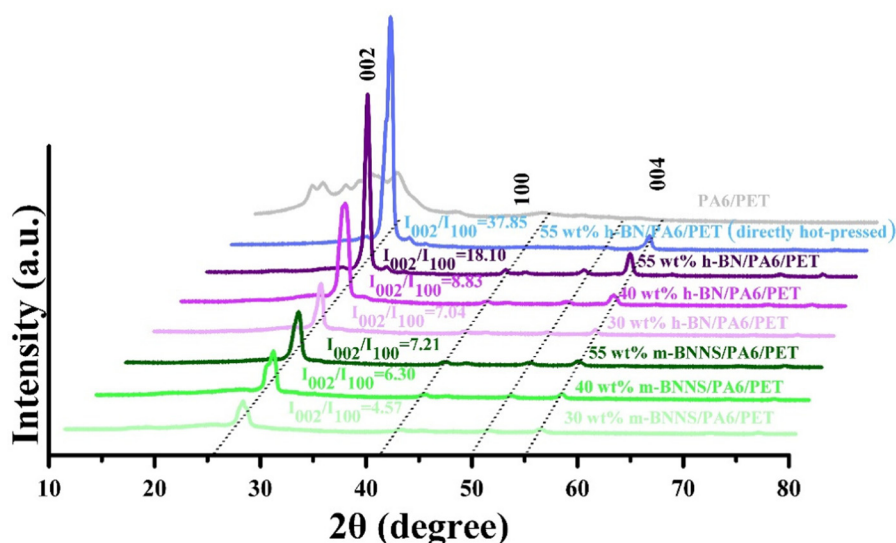

Fig. 6 XRD patterns of the PA6/PET film, h–BN/PA6/PET (directly hot-pressed) composite film, h–BN/PA6/PET composite films, and m–BNNS/PA6/PET composite films.
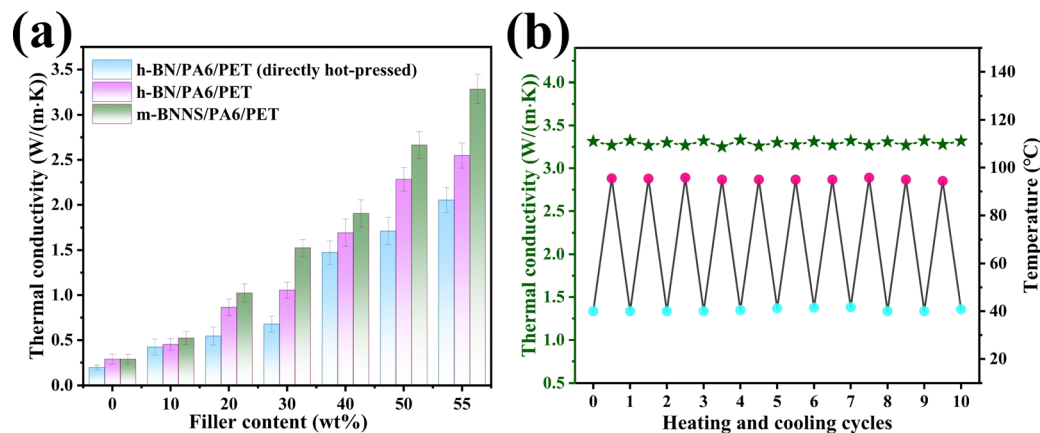
Fig. 7 (a) Thermal conductivities of h-BN/PA6/PET (directly hot-pressed), h-BN/PA6/PET, and m-BNNS/PA6/PET composite films with different filler loading; and (b) under multiple heating/cooling cycles of m-BNNS/PA6/PET composite film at filler loading of 55 wt%.

function of cooling time. In Fig. 8(c) and (d), there was more rapid cooling for the m-BNNS/PA6/PET composite as compared to the other two during the heat dissipation process. These findings indicate the high thermal conductivity and excellent heat dissipation ability of the m-BNNS/PA6/PET composites, which is in accordance with the predictions in Fig. 7(a). Fig. 9(a) shows the TGA curve of the thermally conductive m-BNNS/PA6/PET composite films. With the increase in filler content, the $T_{5\%}$, $T_{30\%}$, and T_{max} values for the m-BNNS/PA6/PET composite films were higher than 376.83 °C, 405.11 °C, and 410.05 °C, respectively, indicating their excellent thermal stability. T_{HRI} is the thermal resistance index of the sample,[68,69] which reveals the parameter of thermal stability of the composites.

The composite's T_{HRI} is greater than 192.96 °C and reaches 211.11 °C at a filler loading of 55 wt%. The first reason for this is that the addition of inorganic fillers increases the thermal degradation resistance. The second reason is that the organic silanol enhances the bonding force between m-BNNSs and PA6/

PET, which increases the thermal stability of the composite. Fig. 9(b) shows the influence of filler loading on the glass transition temperature (T_g) and melting temperature (T_m) of the matrix in m-BNNS/PA6/PET composite film. With the increase in filler content, T_g and T_m of PET increased from 76.13 °C and 244.8 °C to 85.83 °C and 250.00 °C, respectively, while T_g and T_m of PA6 increased from 67.30 °C and 217.58 °C to 71.54 °C and 220.97 °C, respectively. This can be attributed to the fact that the m-BNNSs obstruct the molecular chain movement and rotation of the matrix.

3.4 NEMD simulations

Fig. 10(a) shows the change in G_k for the BNNS/PA6/PET composites. The G_k increases from 67.28 ± 7.15 to 150.58 ± 6.34 MW m^{-2} K^{-1} as the BNNS layers perpendicular to the heat flux direction increase from 2 to 8 layers, respectively, which is consistent with previous studies.[70,71] The G_k is obviously
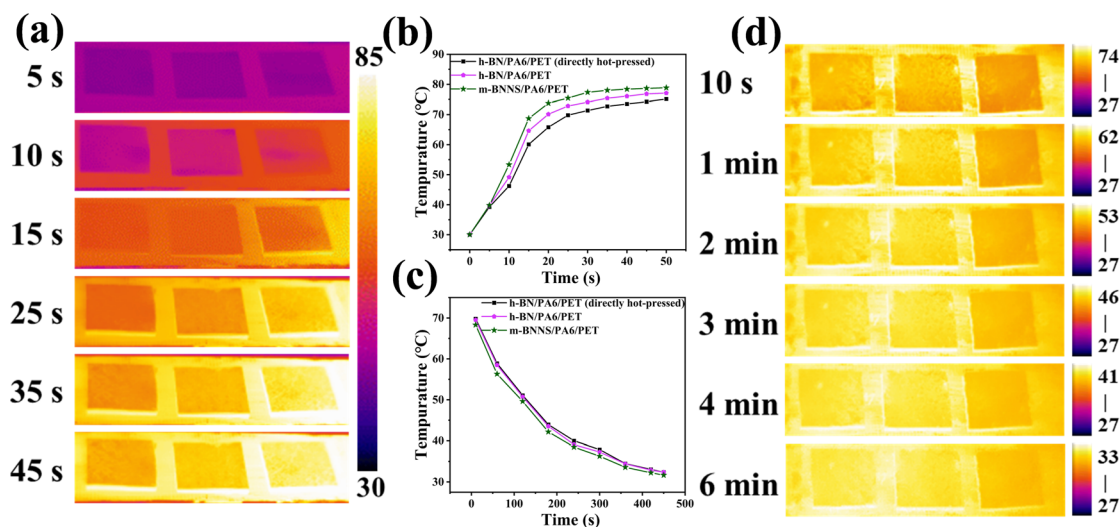

Fig. 8 Infrared images of h-BN/PA6/PET (directly hot-pressed), h-BN/PA6/PET, and m-BNNS/PA6/PET composite film at filler loading of 55 wt% during (a) heating, (b) surface temperature variation with heating time, (c) cooling, and (d) surface temperature variation with cooling time.
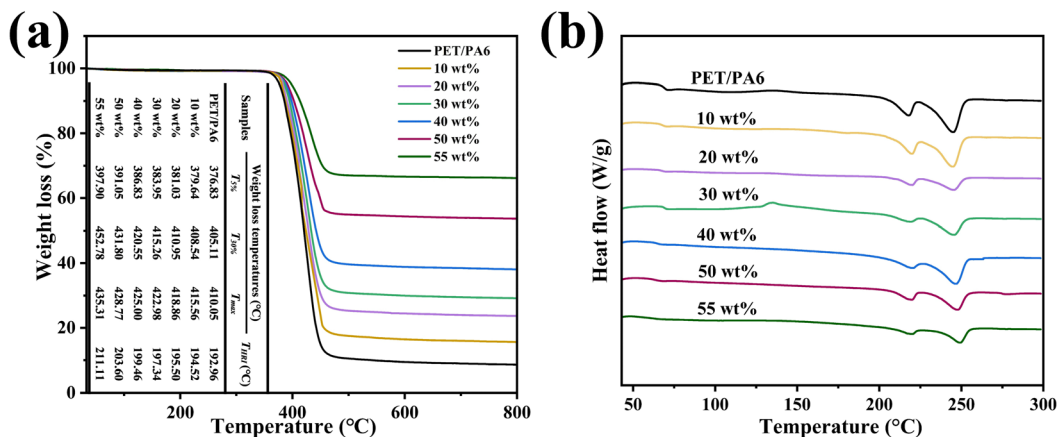
Fig. 9 TGA (a) and DSC (b) curves of the m-BNNS/PA6/PET composite films.

improved when the number of BNNS layers changes from four to six. As the number of BNNS layers exceeds 6, the G_k of the system tends to remain stable. Significantly, as the 8-layer BNNS changes from the vertical heat flux direction to the parallel heat flux direction, the G_k suddenly increases from 150.58 ± 6.34 to 235.43 ± 5.34 MW m^{-2} K^{-1}, which is similar to the findings of previous studies.[72] With the increase in the filler orientation angle from $0°$ to $90°$, the thermal conductivity gradually increases and reaches a maximum at $90°$. This mainly occurred because when heat flows through the interface parallel to the BNNS plane, there are fewer atoms in the interface and less energy loss, leading to an increase in thermal conductivity. To explore the internal mechanism leading to the change in G_k, the projected density of states (PDOS)[73,74] of

BNNSs and PA6/PET atoms were analyzed in this study. The PDOS was calculated from the Fourier transform of the velocity autocorrelation function (VACF):

$$\text{PDOS}(\omega) = \int_{-\infty}^{+\infty} e^{i\omega t}\gamma(t)dt \quad (4)$$

where ω is the frequency and PDOS(ω) denotes the total PDOS at the vibrational frequency ω, and $\gamma(t)$ is normalized VACF:

$$\gamma(t) = \frac{1}{N}\sum_{i=1}^{N}\langle \nu_i(0)\nu_i(t)\rangle \quad (5)$$

where $\nu_i(t)$ and $\nu_i(0)$ are the atomic velocity at time t and 0, respectively. N is the number of atoms in the system. $\langle\cdots\rangle$
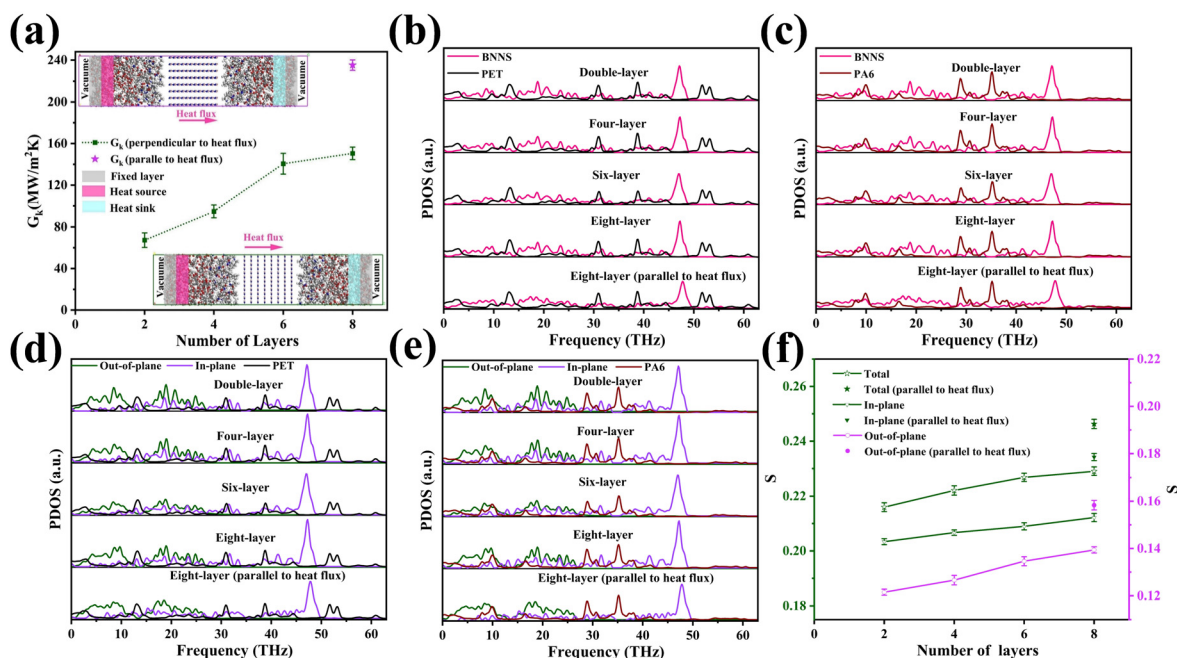

Fig. 10 (a) Interfacial thermal conductance of different systems as a function of the number of layers and orientation; (b) PDOS of BNNSs and PET; (c) PDOS of BNNSs and PA6; (d) out-of-plane and in-plane PDOS of BNNSs and PET; (e) out-of-plane and in-plane PDOS of BNNSs and PA6; (f) the dependences of overlap of the total, out-of-plane, and in-plane PDOS between BNNSs and PET.

denotes the statistical average over multiple time origins. The velocity was correlated every 5 fs with a total integration time of 15 ps. As shown in Fig. 10(b) and (c), the PDOS characteristic peaks of BNNSs mainly appear at 18.5 and 47.3 TH$_Z$, and are consistent with values obtained in the literature,[53,71,75] while those of PET are located at frequencies of approximately 10–15, 32, 38, and 50–55 TH$_Z$, and those of PA6 are located at frequencies of approximately 7–11, 27–30, and 35 TH$_Z$. Compared with BNNSs perpendicular to the heat flux direction, the PDOS of BNNSs parallel to the heat flux direction is smoother and softer, which indicates that the degree of phonon scattering is reduced. The peak at 47.3 THz significantly decreased, while a new peak was generated between 52.3 THz and 55.4 THz. This high-frequency peak was derived from the isolated B and N atoms on the edge of BNNSs that are fully exposed to the heat flow, which can promote the interaction of phonons and then enhance the interfacial heat transfer.[52]

The PDOS overlap region of BNNSs and PA6/PET is mainly distributed over 0–45 THz. In addition, the PDOS of BNNSs can be divided into the in-plane and out-of-plane values, as shown in Fig. 10(d) and (e). There was a wide distribution range for the in-plane PDOS of BNNSs, while the out-of-plane PDOS was mainly distributed in the low frequency region. To quantify the overlap of the PDOS spectra for BNNSs and PA6 or PET, a correlation factor S was introduced,[53] which is defined as:

$$S = \int_0^\infty \min\{P_{\text{BNNS}}(\omega)\}, \{P_{\text{matrix}}(\omega)\}\mathrm{d}\omega \qquad (6)$$

where $P_{\text{BNNS}}(\omega)$, $P_{\text{matrix}}(\omega)$ are the two PDOS of BNNSs and PET or PA6 at frequencies of ω, respectively; min and denotes the lower of the two values. In general, a large S indicates a high degree of overlap, and a high degree of overlap indicates high thermal conductance; otherwise, the opposite. Fig. 10(d) shows that as the number of BNNS layers perpendicular to the heat flux direction increases, the total overlap S, in-plane overlap S, and out-of-plane overlap S all gradually increase. However, the out-of-plane overlap S increases much more than the in-plane overlap. This proves that out-of-plane phonons play a dominant role in the thermal transport of BNNSs.

When the 8-layer BNNS changed from the vertical heat flux direction to the parallel heat flux direction, the total, out-of-plane, and in-plane overlap S all significantly increased. The maximum growth rate of the out-of-plane overlap S was 14%. In addition, the total, out-of-plane, and in-plane overlap S between BNNSs and PA6 varied from 0.2071, 0.1574 and 0.1738 to 0.2238, 0.1862 and 0.1942, respectively. The improved out-of-plane overlap S indicated that the phonon vibrational coupling between BNNSs and PA6/PET was enhanced, which is more conducive to the mutual migration and propagation of phonons. Because modeling the BNNSs with random orientation is challenging, only two distributions, parallel and perpendicular, were studied. The experimental component also shows that many BNNSs with random orientation are in the vertical state. In turn, it can be inferred that BNNSs randomly oriented in the matrix can effectively increase the thermal conductivity.

4. Conclusions

Two-dimensional m-BNNSs obtained by ultrasonic exfoliation of micro h-BN and ternary blend organic silanol modification were randomly distributed in a PA6/PET matrix by a rapid solidification method including solution mixing, rapid solidification, and hot pressing. Compared with the directly hot-pressed composite film, m-BNNSs in a rapidly solidified m-BNNS/PA6/PET composite existed in a randomly orientated state and initiated a heat transfer pathway in a parallel heat flux direction. The filler loading was at 55 wt%, and the thermal conductivity of m-BNNS/PET/PA6 composites was 3.28 W (m^{-1} K^{-1}), which was 64% and 30% higher than that of the h-BN/PET/PA6 (directly hot-pressed) and unmodified h-BN/PET/PA6 composites, respectively.

Our results show that the random orientation and exfoliation and modification of filler were beneficial for increasing the thermal conductivity of the composite. With the increase in filler, m-BNNS/PA6/PET composite film exhibited excellent thermal stability and higher T_{HRI}, T_g, and T_m than the pure PA6/PET matrix. More interestingly, NEMD simulation showed that the increase in the number of BNNS layers and the change in BNNS orientation from vertical heat flux to parallel heat flux can improve the overlap S of PDOS between BNNSs and PA6/PET, and promote phonon coupling. The increase in overlap S is mainly derived from the enhancement of BNNS out-of-plane phonon vibration. At the microscopic scale, NEMD simulation proved that the randomly distributed BNNSs in this experiment are more favorable for improving the out-of-plane thermal conductivity of the composite films.

Author contributions

Qingchong Xu: conceptualization, formal analysis, methodology, visualization, software, data curation, writing – original draft. Zhenxing Chen: conceptualization, project administration, resources, supervision, writing – review & editing, funding acquisition. Xinxin Li, Jiaxin Hu, Yanling Liao, Yongfeng Liu, Long Li, Shiyang Wei: investigation, formal analysis, validation. Ziwei Li: software, visualization, supervision.

Conflicts of interest

The authors declare that they have no known competing financial interests or personal relationships that could have appeared to influence the work reported in this paper.

Acknowledgements

References

1 F. Jiang, N. Song, R. Ouyang and P. Ding, *ACS Appl. Mater. Interfaces*, 2021, **13**, 7556–7566.
2 X. Yang, Y. Guo, Y. Han, Y. Li, T. Ma, M. Chen, J. Kong, J. Zhu and J. Gu, *Composites, Part B*, 2019, **175**, 107070.

3 Y. Guo, K. Ruan and J. Gu, *Mater. Today Phys.*, 2021, **20**, 100449.

4 C. Y. Zhao, Y. B. Tao and Y. S. Yu, *Energy*, 2022, **242**, 123033.

5 Y. Ren, L. Ren, J. Li, R. Lv, L. Wei, D. An, M. Maqbool, S. Bai and C. Wong, *Compos. Sci. Technol.*, 2020, **199**, 108340.

6 H. Guo, T. Xu, S. Zhou, F. Jiang, L. Jin, N. Song and P. Ding, *Composites, Part B*, 2021, **212**, 108716.

7 Y. Ren, Y. Zhang, H. Guo, R. Lv and S. Bai, *Composites, Part A*, 2019, **126**, 105578.

8 C. Liang, H. Qiu, Y. Han, H. Gu, P. Song, L. Wang, J. Kong, D. Cao and J. Gu, *J. Mater. Chem. C*, 2019, **7**, 2725–2733.

9 W. Si, J. Sun, X. He, Y. Huang, J. Zhuang, J. Zhang, V. Murugadoss, J. Fan, D. Wu and Z. Guo, *J. Mater. Chem. C*, 2020, **8**, 3463–3475.

10 Y. Guo, G. Xu, X. Yang, K. Ruan, T. Ma, Q. Zhang, J. Gu, Y. Wu, H. Liu and Z. Guo, *J. Mater. Chem. C*, 2018, **6**, 34–315.

11 M. Hao, Z. Hu, Y. Huang, X. Qian, Z. Wen, X. Wang, L. Liu, F. Lu and Y. Zhang, *Composites, Part B*, 2022, **229**, 109468.

12 A. Skogberg, S. Siljander, A. Mäki, M. Honkanen, A. Efimov, M. Hannula, P. Lahtinen, S. Tuukkanen, T. Björkqvist and P. Kallio, *Nanoscale*, 2022, **14**, 448–463.

13 X. Liu, Z. Wang, J. Sun, Z. Zhao, S. Zhan, Y. Guo, H. Zhou, W. Liu, J. Wang and T. Zhao, *Compos. Sci. Technol.*, 2021, **202**, 108558.

14 Z. Wei, W. Xie, B. Ge, Z. Zhang, W. Yang, H. Xia, B. Wang, H. Jin, N. Gao and Z. Shi, *Compos. Sci. Technol.*, 2020, **199**, 108304.

15 W. Lee and J. Kim, *Composites, Part B*, 2022, **230**, 109526.

16 G. Han, X. Zhao, Y. Feng, J. Ma, K. Zhou, Y. Shi, C. Liu and X. Xie, *Chem. Eng. J.*, 2021, **407**, 127099.

17 X. Zhang, H. Zhang, D. Li, H. Xu, Y. Huang, Y. Liu, D. Wu and J. Sun, *Composites, Part B*, 2021, **224**, 109207.

18 L. Zhao, L. Wang, Y. Jin, J. Ren, Z. Wang and L. Jia, *Composites, Part B*, 2022, **229**, 109454.

19 J. Wie, M. Kim and J. Kim, *Appl. Surf. Sci.*, 2020, **529**, 147091.

20 C. Xiao, Y. Guo, Y. Tang, J. Ding, X. Zhang, K. Zheng and X. Tian, *Composites, Part B*, 2020, **187**, 107855.

21 Y. Qin, B. Wang, X. Hou, L. Li, C. Guan, Z. Pan, M. Li, Y. Du, Y. Lu, X. Wei, S. Xiong, G. Song, C. Xue, W. Dai, C. Lin, J. Yi, N. Jiang and J. Yu, *Compos. Commun.*, 2022, **29**, 101008.

22 S. Cheng, X. Duan, X. Liu, Z. Zhang, D. An, G. Zhao and Y. Liu, *J. Mater. Chem. C*, 2021, **9**, 7127–7141.

23 C. Yu, W. Gong, W. Tian, Q. Zhang, Y. Xu, Z. Lin, M. Hu, X. Fan and Y. Yao, *Compos. Sci. Technol.*, 2018, **160**, 199–207.

24 N. Sun, J. Sun, X. Zeng, P. Chen, J. Qian, R. Xia and R. Sun, *Composites, Part A*, 2018, **110**, 45–52.

25 H. Yu, P. Guo, M. Qin, G. Han, L. Chen, Y. Feng and W. Feng, *Compos. Sci. Technol.*, 2022, **222**, 109406.

26 D. Liu, H. Chi, C. Ma, M. Song, P. Zhang and P. Dai, *Compos. Sci. Technol.*, 2022, **220**, 109292.

27 B. Ghosh, F. Xu, D. M. Grant, P. Giangrande, C. Gerada, M. W. George and X. Hou, *Adv. Electron. Mater.*, 2020, **6**, 2000627.

28 X. Wang and P. Wu, *ACS Appl. Mater. Interfaces*, 2019, **11**, 28943–28952.

29 C. Yu, J. Zhang, Z. Li, W. Tian, L. Wang, J. Luo, Q. Li, X. Fan and Y. Yao, *Composites, Part A*, 2017, **98**, 25–31.

30 Y. He, F. Kuang, Z. Che, F. Sun, K. Zheng, J. Zhang, X. Cao and Y. Ma, *Composites, Part A*, 2022, **157**, 106933.

31 S. Wei, Q. Yu, Z. Fan, S. Liu, Z. Chi, X. Chen, Y. Zhang and J. Xu, *RSC Adv.*, 2018, **8**, 22169–22176.

32 F. Wu, S. Chen, X. Tang, H. Fang, H. Tian, D. Li and X. Peng, *Compos. Sci. Technol.*, 2020, **197**, 108245.

33 C. Pan, K. Kou, Y. Zhang, Z. Li and G. Wu, *Composites, Part B*, 2018, **153**, 1–8.

34 Y. Chen, X. Hou, M. Liao, W. Dai, Z. Wang, C. Yan, H. Li, C. Lin, N. Jiang and J. Yu, *Chem. Eng. J.*, 2020, **381**, 122690.

35 Q. Ma, Z. Wang, T. Liang, Y. Su, J. Li, Y. Yao, X. Zeng, Y. Pang, M. Han, X. Zeng, J. Xu, L. Ren and R. Sun, *Composites, Part A*, 2022, **157**, 106904.

36 H. Cheng, K. Zhao, Y. Gong, X. Wang, R. Wang, F. Wang, R. Hu, F. Wang, X. Zhang, J. He and X. Tian, *Composites, Part A*, 2020, **137**, 106026.

37 Y. Zhang, H. He, B. Huang, S. Wang and X. He, *Compos. Sci. Technol.*, 2021, **208**, 108766.

38 Y. Liu, Z. Chen, Y. Shen, Y. Zhou, D. Wang, Z. Lei, W. Feng and Z. Min, *Mater. Lett.*, 2020, **261**, 127002.

39 M. T. Huang and H. Ishida, *J. Polym. Sci., Part B: Polym. Phys.*, 1999, **37**, 2360–2372.

40 Z. Liu, J. Li and X. Liu, *ACS Appl. Mater. Interfaces*, 2020, **12**, 6503–6515.

41 Q. Yan, W. Dai, J. Gao, X. Tan, L. Lv, J. Ying, X. Lu, J. Lu, Y. Yao, Q. Wei, R. Sun, J. Yu, N. Jiang, D. Chen, C. Wong, R. Xiang, S. Maruyama and C. Lin, *ACS Nano*, 2021, **15**, 6489–6498.

42 G. Zhao, F. Zhang, Y. Wu, X. Hao, Z. Wang and X. Xu, *Adv. Opt. Mater.*, 2016, **4**, 141–146.

43 J. Ren, L. Stagi and P. Innocenzi, *J. Mater. Sci.*, 2021, **56**, 4053–4079.

44 Q. Wang, D. J. Keffer, S. Petrovan and J. B. Thomas, *J. Phys. Chem. B*, 2010, **114**, 786–795.

45 S. Chen, L. Gorbatikh and D. Seveno, *ACS Appl. Nano Mater.*, 2021, **4**, 10799–10809.

46 X. Yang, X. Wang, W. Wang, Y. Fu and Q. Xie, *Int. J. Heat Mass Transfer*, 2020, **159**, 120105.

47 Q. L. Xiong and S. A. Meguid, *Eur. Polym. J.*, 2015, **69**, 1–15.

48 J. Choi, H. Shin and M. Cho, *Polymer*, 2016, **89**, 159–171.

49 S. M. Rahimian-Koloor, H. Moshrefzadeh-Sani, S. M. Hashemianzadeh and M. M. Shokrieh, *Curr. Appl. Phys.*, 2018, **18**, 559–566.

50 Y. Tsuji, Y. Kitamura, M. Someya, T. Takano, M. Yaginuma, K. Nakanishi and K. Yoshizawa, *ACS Omega*, 2019, **4**, 4491–4504.

51 Z. Li, K. Li, J. Liu, S. Hu, S. Wen, L. Liu and L. Zhang, *Polymer*, 2019, **177**, 262–273.

52 W. Zhang, H. Li, H. Jiang, H. Wu, Y. Lu, X. Zhao, L. Liu, Y. Gao and L. Zhang, *Langmuir*, 2021, **37**, 12038–12048.

53 T. Liang, M. Zhou, P. Zhang, P. Yuan and D. Yang, *Int. J. Heat Mass Transfer*, 2020, **151**, 119395.

54 L. Lindsay and D. A. Broido, *Phys. Rev. B*, 2011, **84**, 155421.

55 Y. Wang, Z. Chang, K. Gao, Z. Li, G. Hou, J. Liu and L. Zhang, *Polymer*, 2021, **224**, 123697.

56 M. Wang, N. Hu, L. Zhou and C. Yan, *Carbon*, 2015, **85**, 414–421.

57 T. Luo and J. R. Lloyd, *Adv. Funct. Mater.*, 2012, **22**(10), 2495–2502.

58 C. Chang, S. Ju, J. Chang, S. Huang and H. Yang, *RSC Adv.*, 2014, **4**, 26074.

59 K. Wu, P. Liao, R. Du, Q. Zhang, F. Chen and Q. Fu, *J. Mater. Chem. A*, 2018, **6**, 11863–11873.

60 G. Han, D. Zhang, C. Kong, B. Zhou, Y. Shi, Y. Feng, C. Liu and D. Wang, *Chem. Eng. J.*, 2022, **437**, 135482.

61 Z. Liu, J. Li and X. Liu, *ACS Appl. Mater. Interfaces*, 2020, **12**, 6503–6515.

62 M. G. Rasul, A. Kiziltas, C. D. Malliakas, R. Rojaee, S. Sharifi-Asl, T. Foroozan, R. Shahbazian-Yassar and B. Arfaei, *Compos. Sci. Technol.*, 2021, **204**, 108631.

63 Z. Zhu, C. Li, E. Songfeng, L. Xie, R. Geng, C. Lin, L. Li and Y. Yao, *Compos. Sci. Technol.*, 2019, **170**, 93–100.

64 X. Tian, N. Wu, B. Zhang, Y. Wang, Z. Geng and Y. Li, *Chem. Eng. J.*, 2021, **408**, 127360.

65 Q. Cai, D. Scullion, A. Falin, K. Watanabe, T. Taniguchi, Y. Chen, E. J. G. Santos and L. H. Li, *Nanoscale*, 2017, **9**, 3059–3067.

66 M. Guan, Z. Li, L. Hao, M. Zhou, L. Chen, H. Chen, H. Zhou and X. Zhou, *Chem. Eng. J.*, 2021, **423**, 130166.

67 L. Wang, Y. Bai, Z. Ma, C. Ge, H. Guan and X. Zhang, *SN Appl. Sci.*, 2021, **3**, 1–10.

68 J. Gu, Z. Lv, Y. Wu, Y. Guo, L. Tian, H. Qiu, W. Li and Q. Zhang, *Composites, Part A*, 2017, **94**, 209–216.

69 X. Yang, Y. Guo, Y. Han, Y. Li, T. Ma, M. Chen, J. Kong, J. Zhu and J. Gu, *Composites, Part B*, 2019, **175**, 107070.

70 R. Ma, X. Wan, T. Zhang, N. Yang and T. Luo, *ACS Omega*, 2018, **3**, 12530–12534.

71 X. Yang, X. Wang, W. Wang, Y. Fu and Q. Xie, *Int. J. Heat Mass Transfer*, 2020, **159**, 120105.

72 J. Gao, H. Wu, A. Li, Y. Yue, D. Xie and X. Zhang, *ACS Appl. Nano Mater.*, 2019, **2**, 6828–6835.

73 X. Ma, S. Wu, Z. Yi, D. Peng and J. Zhang, *Int. J. Heat Mass Transfer*, 2019, **137**, 790–798.

74 M. An, H. Wang, Y. Yuan, D. Chen, W. Ma, S. W. Sharshir, Z. Zheng, Y. Zhao and X. Zhang, *Surf. Interfaces*, 2022, **28**, 101690.

75 X. Li, Y. Li, M. M. Alam, J. Miao, P. Chen, R. Xia, B. Wu and J. Qian, *J. Mater. Chem. C*, 2020, **8**, 9569–9575.